

Single-cell motion of magnetotactic bacteria in microfluidic confinement: interplay between surface interaction and magnetic torque

Agnese Codutti[‡] 1 2 3, Mohammad A. Charsooghi[‡] 1 6, Elisa Cerdá-Doñate[‡] 1, Hubert M. Taïeb 1, Tom Robinson* 2, Damien Faivre* 1 4, Stefan Klumpp* 2 5

[‡] first authors

* corresponding author

1 Biomaterials department, Max Planck Institute of Colloids and Interfaces, Potsdam, Germany

2 Theory and Bio-systems department, Max Planck Institute of Colloids and Interfaces, Potsdam, Germany

3 Biological physics and Morphogenesis group, Max Planck Institute of Dynamics and Self-Organization, Göttingen, Germany

4 Aix Marseille Université, CNRS, CEA, BIAM, 13108 Saint Paul lez Durance, France

5 Institute for the Dynamics of Complex Systems, University of Göttingen, Göttingen, Germany

6 Department of Physics, Institute for Advanced Studies in Basic Sciences (IASBS), Zanjan 45137-66731, Iran

Abstract

Swimming microorganisms often experience complex environments in their natural habitat. The same is true for microswimmers in envisioned biomedical applications. The simple aqueous conditions typically studied in the lab differ strongly from those found in these environments and often exclude the effects of small volume confinement or the influence that external fields have on their motion. In this work, we investigate magnetically steerable microswimmers, specifically magnetotactic bacteria, in strong spatial confinement and under the influence of an external magnetic field. We trap single cells in micrometer-sized microfluidic chambers and track and analyze their motion, which shows a variety of different trajectories, depending on the chamber size and the strength of the magnetic field. Combining these experimental observations with simulations using a variant of an active Brownian particle model, we explain the variety of trajectories by the interplay between the wall interactions and the magnetic torque. We also analyze the pronounced cell-to-cell heterogeneity, which makes single-cell tracking essential for an understanding of the motility

patterns. In this way, our work establishes a basis for the analysis and prediction of microswimmer motility in more complex environments.

Introduction

Microswimmers and other self-propelled microscopic particles have received extensive attention in recent years, both directed towards the fundamental physical principles of their propulsion mechanisms and their rich collective behavior^{1–3}, and towards their potential for environmental and biomedical applications including as drug carriers, infertility cures, bioremediation, or MRI imaging^{4–13}. Envisioned applications of microswimmers often imply their use in complex environments that may present a variety of obstacles, confinement to pores, fluid flows, complex fluids or other complications^{7,11} compared to the motion in simple aqueous solutions that is typical under lab conditions^{14–16}. The same is true for the environments that form the natural habitats of microorganisms that are studied as biological or hybrid microswimmers, and include sediments, soils, as well as the natural habitats within the bodies of animals and humans^{8,17–23}. Several recent studies have therefore started to address their motion in complex environments such as model porous systems and confined spaces using microfluidic devices; for example using arrays of pillars^{24,25}, ratchet-like sorting devices^{26–28}, or droplets²⁹.

One situation of particular interest is the confinement of microswimmers to a small space. In this case, the steric and hydrodynamic interactions with the confining walls have a strong impact on the motility and swimmer trajectories²². Moreover, some microorganisms show behavioral responses to collision with surfaces, for example by changing their mode of self-propulsion³⁰. The effect of confinement on their behavior can be studied using microfluidic devices that trap microswimmers for extended observation of individual swimmers, which allow us to study the effect of various parameters such as changes in magnetic field on the same bacterium. However, few such studies have been reported so far. One notable exception is a recent study of the alga *Chlamydomonas reinhardtii*, which was observed to swim along the wall and to accumulate in regions with a large wall curvature³¹. However, this report only focused on a dumbbell shape model to represent the wall steric interaction, which is not always applicable to different swimmers due to the variety of cell shapes and swimming patterns (pusher or puller type for example).

The tactic behavior of microorganisms is known to help their navigation and proliferation in complex environments. Accordingly, a line of research has also developed, which seeks to understand the directionality of microswimmers and how to control them due to their tactic behaviors or due to interactions with external fields^{8,32,33}. This regard, magnetic fields are particularly interesting, as they

allow the remote steering of microswimmers exhibiting a magnetic moment, a feature suitable for the remote control of the swimmers performing biomedical tasks in the human body ⁷. Such microswimmers include magnetotactic bacteria ^{34–36}, i.e. bacteria equipped with a magnetic moment due to dedicated organelles, the magnetosomes, as well as biohybrid and synthetic magnetic swimmers ^{7,37–41}. The use of magnetic microswimmers in small confined spaces such as microfluidic traps opens the possibility to study the interplay of confinement and directionality imposed by the external magnetic field. An understanding of this interplay is crucial to understand the navigation of biological microswimmers in complex environments as well as to develop strategies for steering microswimmers through such environments.

Here, we therefore investigate the swimming of the magnetotactic bacterium *Magnetospirillum gryphiswaldense* (MSR-1) confined to circular traps, both in the presence and absence of an external magnetic field that guides the swimming directionality. To that end, we designed a microfluidic trapping platform, featuring actuable elastomeric PDMS membranes to create defined micrometer-sized containers. This approach allows us to observe and track individual bacteria for extended periods of time and to account for considerable heterogeneities in their physical properties and swimming behaviors. Single-cell analysis allows us to pinpoint the main characteristics determining the trajectories, which would otherwise be lost and averaged out in a cell population approach. We complement our experimental investigation with simulations using a variant of an active Brownian particle model, providing an effective general model to describe the complex wall-bacterium interaction. Combining the experimental results with the simulations allows us to explain the variety of observed behaviors by the interplay of two torques, induced on the one hand by the magnetic field and on the other hand by the interaction with the confining walls. Overall, our approach combining microfluidic trapping, observation of individual swimmers, and interpretation of the observations with the help of modeling, provides a path towards understanding and predicting swimmers in other, more complex environments.

Results

Microfluidic trapping of single bacteria

Confining individual bacteria in a small, closed volume provides an opportunity to study the motility of individual bacteria by long-time observation of the same cell. Microfluidics offers the possibility of microfabricating such small features on a length-scale similar to that of a single cell, thus emphasizing their interactions with the confining walls. However, constructing a well-defined and reproducible volume that is sealable is challenging. Previous approaches such as the so called ‘Quake’s valves’⁴² or donut-shaped valves⁴³ are not applicable as they result in edges where bacteria can become permanently trapped, or generate volumes well beyond a single-cell size, respectively. Therefore, we developed a microfluidic trapping system based on a pressure actuated ceiling (Fig. 1) to trap and study individual magnetotactic bacteria. In this multilayer microfluidic strategy, a bacterial solution is placed inside a microfluidic channel whose ceiling (a PDMS membrane) is patterned with open cylinders (Supplementary Fig. 2c). Due to the elastic properties of thin PDMS membranes, when a downward force is applied on the patterned ceiling, it gets displaced towards the bottom of the channel. This results in the cylinders becoming sealed (i.e. traps), resulting in the confinement of bacteria inside them (Fig. 1 A and B). The circular design was fabricated directly into the channel ceiling for size reproducibility and control, thus ensuring a 2-D environment where we can tune the trap dimensions to influence the swimming behavior (i.e. diameter).

Single bacteria were isolated in circular microfluidic traps of different dimensions with radii of 7.5, 12.5, 17.5, 25 and 45 μm . The trap size is reproducible up to a variability in the radii of 1 to 2 μm (see “Materials and methods - Microfluidic trap characterization” and Supplementary Table 1). The height of the trap is fixed at 10 μm , limiting the motion to the x-y plane and providing simple, quasi-2D trajectories. Successful confinement of individual bacteria in these microfluidic traps allowed us to image the same cell for up to one hour. Fig. 1c shows the histogram of the number of trapped bacteria for different cell concentrations (given by the optical density OD_{565}). In this work, we aimed at characterizing the motion of individual bacteria, therefore the cell concentration was adjusted ($\text{OD}=0.03 - 0.05$) such that on average one bacterium is trapped in the smaller microfluidic traps (from 7.5 to 25 μm radius) and 2-3 bacteria in the largest one (45 μm) (see Supplementary Fig. 3). Fig. 1d shows a typical trajectory of a bacterium in the microfluidic trap of 45 μm in the absence of any magnetic field (ambient magnetic field is cancelled out, see “Materials and methods - Microscopy and image stabilization”; trajectories in smaller microfluidic traps are shown in Supplementary Fig. 4, a representative movie in Supplementary Video 1). Because the bacterium swims very close to the wall, an image stabilization and a background subtraction processing was implemented to track the motion

(see “Materials and methods - Microscopy and image stabilization”), but even with these improvements the tracking algorithm cannot track the bacterium continuously. Therefore, continuous fragments (43 ± 16 fragments) of trajectories are shown in different colors in Fig. 1d.

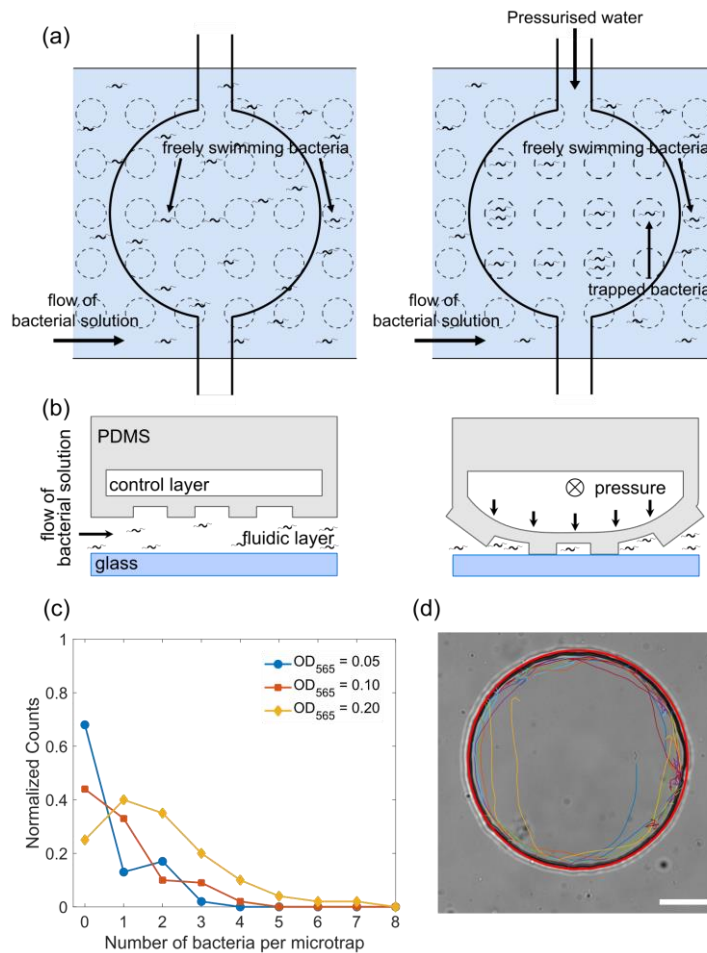


Fig. 1. Trapping and tracking of bacteria in microfluidic traps: (a) Schematic top view of how the microfluidic trap system achieves confinement of bacteria using multiple layers: a fluidic layer (bottom layer) and a control layer (top layer). Free bacteria are introduced using the lower fluidic layer and by applying pressure to the top control layer the valve deforms and the bacteria are confined in the micron-sized traps of a defined diameter. (b) Schematic side view of the valve in panel (a), see Material and methods “Fabrication of the master molds and microfluidic systems” and “Operation of the chip” sections for more details. (c) Histogram of the number of bacteria isolated in one microfluidic trap of radius $12.5 \mu m$ at three different bacteria concentrations of OD_{565} 0.05, 0.1, and 0.2. (d) Bright-field microscopy image of a typical $45 \mu m$ radius trap with the extracted trajectory of the bacteria (different segments of the same trajectory are depicted with colored lines). A red circle is fitted to visualize the microfluidic trap perimeter. Scale bar is $20 \mu m$. For more details, see Supplementary Figure 1d).

Motion in confinement

For all microfluidic trap dimensions and in the absence of applied magnetic fields, we observed that bacteria predominantly swim along the walls and only occasionally move to the interior of the trap (Figure 1d). To quantify this behavior, we determined the radial probability distribution functions of the trap occupancy (Figure 2). Swimming along the walls is reflected in a pronounced peak in that distribution, situated within few micrometers from the border of the microfluidic trap (see supplementary Table 2 for the peak position values), and with a broad tail that extends into the center. The observed behavior is similar to the one reported for algae in confinement³¹, even though the bacterium is hydrodynamically different from an alga, since it possesses a spiral shape body^{34,35} instead of a spherical one³¹; two rotating flagella at each pole of the body^{34,35} instead of two beating flagella in the front³¹; and, most probably, displays a pusher and puller dynamic like other biflagellate magnetotactic bacteria⁴⁴ instead of breaststroke swimming³¹.

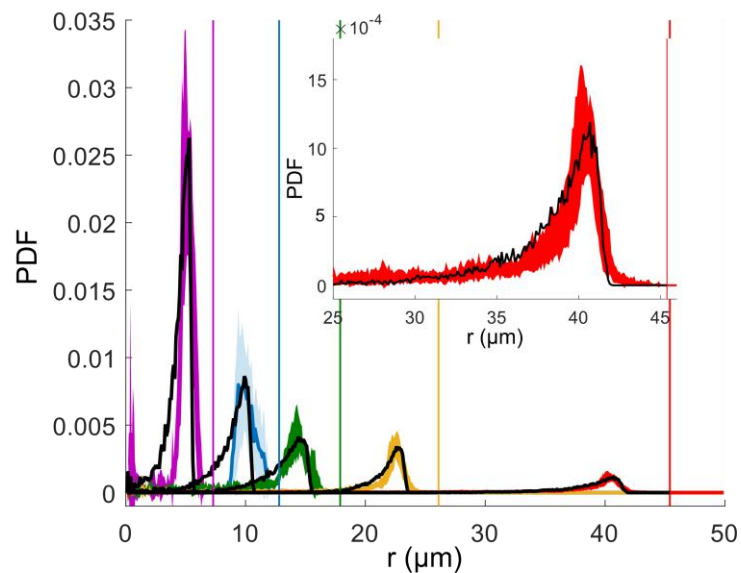


Fig. 2. Mean radial distribution of the bacteria given as a Probability Density Function (PDF) (filled line) with the corresponding standard deviation (colored area) for different microfluidic trap dimensions (trap radius 7.5 μm in violet, 12.5 μm in blue, 17.5 μm in green, 25 μm in yellow and 45 μm in red), and the corresponding wall positions (vertical lines) in the absence of magnetic fields. Each curve is a mean over about 6 different traps. For small traps (7.5, 12.5, and 17.5 μm) with only 1 bacterium, and for 25 μm and 45 μm traps with the maximum number of 2 and 4 bacteria are examined, respectively. The total trajectory points acquired for each bacterium is about 10^4 . The black dotted lines show the corresponding simulated distributions. Insert shows an enlargement of the peak for the biggest microfluidic trap with radius of 45 μm .

Next, we turned to simulations to investigate the mechanism for motion along the walls. We used an active Brownian particle model that describes swimming bacteria as self-propelled particles subjected

to rotational diffusion - a theoretical approach that has been used extensively to study microswimmers and other active particles in general ^{1,45-52}, but also specifically for magnetic swimmers and magnetotactic bacteria^{53,54}. The simulation is three dimensional, with radii and depth to the trap taken from the experimental values. The motion is confined in quasi 2D as a result of the surface interactions (both ceiling, bottom and side walls). Using the measured value for the swimming speed (see Supplementary Table 3), we systematically varied the interactions with the walls and compared the radial distributions from the simulations to the experimental ones. The wall interaction was tuned with two parameters: the interaction range A_w (which gives an indication of the distance from the wall at which hydrodynamics acts and thus mainly influences the peak position) and the strength of an effective wall torque T_w , which reorients the cells upon contact with the walls. In the absence of such wall torque ($T_w = 0$), the peak of the radial distribution is closer to the wall than observed in the experiments (Supplementary Figs. 5 and 6). Simulations resulting from the interactions parameters that give the best match to the experiments (see Supplementary Table 3) are included as the black dotted lines in Fig. 2. The fitted parameters A_w and T_w depend on the microfluidic trap size (thus on the curvature of the trap, see Supplementary Fig. 7), and are used for all following simulations at different magnetic fields but the same size. A similar wall torque was previously used to describe the swimming of algae ³¹ and likely represents the reorientation of the cells due to steric as well as hydrodynamic interactions with the walls. While for algae the torque was derived from an asymmetric dumbbell model ³¹, here we used a more general, phenomenological approach with an effective torque and two free fitting parameters A_w and T_w (see Materials and methods - “Computational modelling” section) that is applicable independent of cell shape, swimming behavior and the specifics of the corresponding hydrodynamics. The Shape of the radial distributions indicate that different swimmers behave similarly in strong confinement, and that this behavior can be effectively described with a general method that ignores the specificity of the hydrodynamics of the swimmer.

Influence of a magnetic field

While the behavior described so far is similar to the previously observed swimming of algae in a circular environment (i.e. with the algae swimming at the wall), here a magnetic field can be used as an additional external control parameter in the case of magnetotactic bacteria. A magnetic field exerts a torque on these bacteria aligning their motion with the direction of the field. The observation of a torque resulting from the interaction with the wall thus suggests the possibility of competing effects, which we studied in both experiments and simulations. Fig. 3 shows how the magnetic field affects the trajectories in the largest microfluidic trap (here, for a bacterium swimming with its magnetic north pole at its front, the typical case in our experiments, as explained in Materials and methods - “Selection

of magnetic motile bacteria”). The magnetic field is oriented such that its north points to the left side of the trap. For a field strength of 50 μT , comparable to the magnetic field of the Earth, the observed trajectories (both experimental and simulated) strongly resemble the ones of the case without magnetic field, and bacteria mostly swim along the wall circling the microfluidic trap. However, when a field of 500 μT is applied, we observe bacteria that perform U-turns inside the trap: i.e. a bacterium in the interior of the trap swims in the direction of the field until it hits the wall, where it continues its path along the wall, therefore turning against the direction of the magnetic field. Eventually, a U-turn realigns the bacterium with the field and moves it away from the wall and back into the interior of the trap. In Fig. 3, we also show the corresponding simulated trajectories (with the same velocity as the experiments, same microfluidic trap size, and with the parameters A_w and T_w determined from the mean radial distribution without magnetic field), which show the same behavior.

We understand the U-turns as reflecting the interplay between the wall torque and the magnetic torque (see also Supplementary Fig. 8). While the direction of the wall torque depends on whether the bacterium swims clockwise or counterclockwise (see Materials and methods - “Computational modelling”), the magnetic torque depends on the magnetic moment orientation and on the swimming direction relative to the magnetic field. As an example, for a bacterium swimming clockwise with the north of its magnet at its front, the wall-interaction torque always points into the quasi 2D surface to which the bacteria are constricted to swim. At the magnetic north of the external field, the magnetic torque is opposite to the wall torque; at the south, the two torques add up (together with random noise) to direct the bacterium away from the wall and into the trap interior.

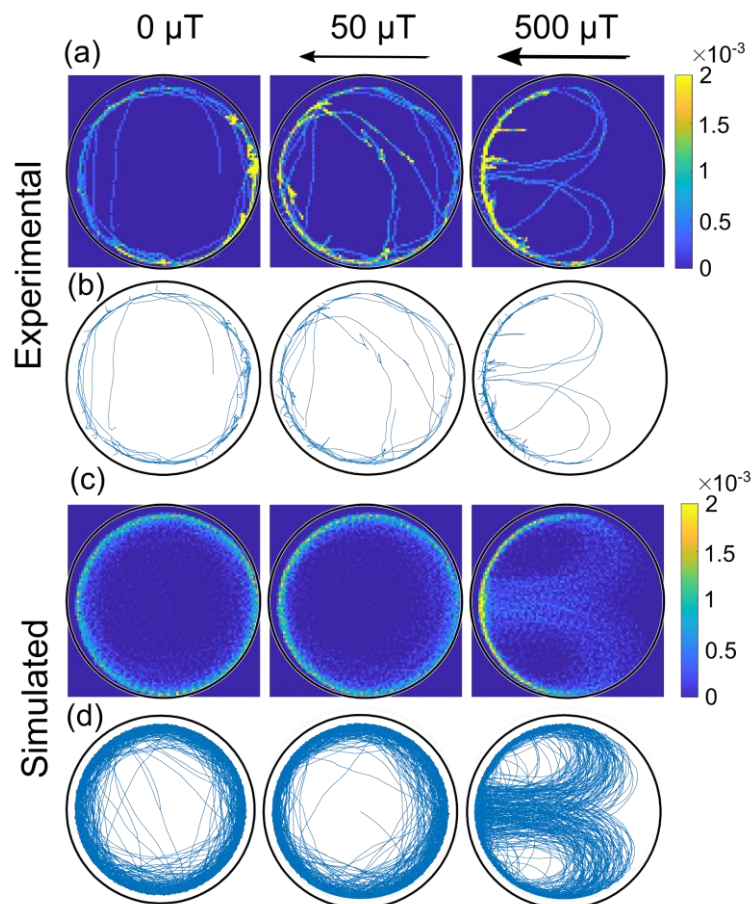


Fig. 3. Comparison of experimental and simulated trajectories in a confined micro-environment. Heat maps (row a and c, $1 \mu\text{m} \times 1 \mu\text{m}$ resolution; the color bar shows the normalized counts) and corresponding trajectories (row b and d) for bacteria swimming with the magnetic north pole in front, at different magnetic fields (0, 50 and 500 μT) in the largest microfluidic trap with a radius of 45 μm . The rows a and b are experimental trajectories (see also Supplementary Video 2) whereas c and d are simulated. Bacteria in both the simulation and experiment move at an average velocity of 40 $\mu\text{m s}^{-1}$.

Motility and cell-to-cell heterogeneity

Using our experimental setup, we observe a variety of different trajectories, even if we analyze bacteria that always swim with their north pole at their front and exclude the rare bacteria that exhibit directional reversals or swim persistently with their south pole at their front. To understand the variety, we simulated different trajectories with different strengths of the magnetic torque (dependent on mB , the product of the magnetic moment m and the magnetic field B) and different swimming velocities v . The diagram in Fig. 4a maps three simulated regimes, characterized by different types of trajectories for the largest microfluidic trap radius (45 μm): For very small swimming velocities, the bacteria are trapped at the north pole of the trap. For intermediate velocities, the bacteria perform the U-turns described above. Finally, for large swimming velocities, they circle around the trap. The transitions between these three behaviors depend on the field strength and can be understood by considering the interplay of different length scales. The transition between U-turns and circling

depends on two length scales: the radius of the microfluidic trap R_{trap} and the radius of the U-turn R_U .

The U-turn radius can be calculated from the balance between the magnetic torque and the rotational friction⁵⁵, which leads to

$$R_U = \frac{\pi \gamma_r}{2 mB} v = \frac{\pi k_B T}{2 m B D_r} v, \quad (1)$$

where γ_r is the rotational friction coefficient, D_r is the rotational diffusion coefficient, k_B is the Boltzmann constant and T is the temperature. Thus, U-turns can only be observed if the U-turn radius is smaller than the microfluidic trap radius, otherwise the trajectories tend to follow the wall. These two regimes are indicated by the green and red areas in Fig. 4a, respectively. The transition between these two behaviors is given by the black line, which represents the points where the U-turn radius is the same as the microfluidic trap radius,

$$\frac{mB}{k_B T} = \frac{\pi v/D_r}{2 R_{\text{trap}}}. \quad (2)$$

We note that this expression relates two dimensionless quantities, the ratio of the magnetic and thermal energies and the ratio of the persistence length of active motion (in the absence of a magnetic field, v/D_r) and the trap size. The transition to the north polar trapping regime (yellow area in Fig. 4a) can also be understood by a comparison of length scales: if the U-turn radius is smaller than the interaction range A_w of the wall, then the bacterium tends to remain on the wall, and spends most of its time at the north pole of the microfluidic trap. This transition is marked by the dashed line in Fig. 4a.

The interplay between these length scales suggested by our theoretical analysis is confirmed by our experimental data. In Fig. 4b, we plot the measured U-turn radius against the measured velocity, pooling data for all microfluidic trap dimensions, for an example case at 500 μT (Fig. 4b). The data points cluster around the theoretical prediction for the U-turns from Eq. (1) (solid line in Fig. 4b), obtained using the mean magnetic moment estimated from TEM images to be $m = 0.36 \times 10^{-3} \text{ A } \mu\text{m}^2$ (see Materials and methods - "Magnetic moment measurement"). The scatter around the theoretical expectation can be attributed to cell-to-cell variability in the magnetic moment, as discussed below. For the biggest microfluidic traps of radii 25 and 45 μm (Fig. 4b), U-turns are observed even for high velocities and low magnetic moments, whereas for smaller microfluidic traps 12.5 and 17.5 μm , only very small U-turn radii are observed and obviously none are bigger than the microfluidic trap size itself. Especially for higher velocities and small microfluidic traps, we can observe U-turns only for bacteria with higher magnetic moments (Supplementary Fig. 9).

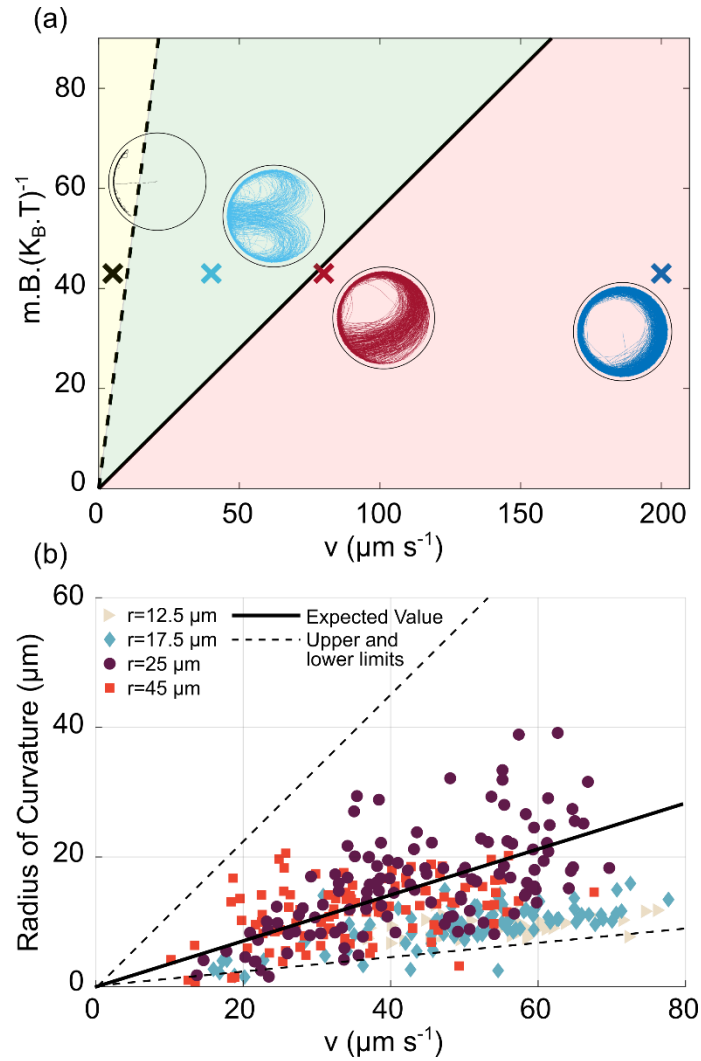


Fig. 4. U-Turn dependence on velocity and magnetic field. a) Phase diagram of the trajectories in the space of $\left(v, \frac{mB}{k_B T}\right)^{-1}$ for the largest microfluidic trap (radius $45 \mu\text{m}$) with a magnetic field pointing to the left. The solid black line is given by Eq. (2) and represents the transition between the red area (for which U-turns are not visible since they are larger than the microfluidic trap radius), and the green area, for which the U-turns are clearly visible. The black dashed line is given by $R_U = A_w$ and represents the transition between the green area and the yellow area, where the trajectories tend to be confined at the wall since the U-turn radius is smaller than the wall-interaction-torque range. The points shown here are taken at $\frac{mB}{k_B T} = 43$ given by the experiment ($B = 500 \mu\text{T}$, $m = 0.36 \times 10^{-3} \text{ A } \mu\text{m}^2$, $T = 305 \text{ K}$). The insets are the corresponding simulations of the trajectory for that region. b) Experimental U-turn radius as a function of the measured velocity for experiments conducted at $500 \mu\text{T}$. Different colors correspond to different microfluidic trap radii r (\blacktriangleright $12.5 \mu\text{m}$, \blacklozenge $17.5 \mu\text{m}$, \blacksquare $25 \mu\text{m}$, \bullet $45 \mu\text{m}$, with no U-turns for the smallest microfluidic trap of radius $7.5 \mu\text{m}$). The black line corresponds to the theoretical prediction $R_U = \frac{\pi}{2} \frac{k_B T}{m B D_r} v$ with $m = 0.36 \times 10^{-3} \text{ A } \mu\text{m}^2$ and $D_r = 0.1 \text{ s}^{-1}$ for a typical micron size microswimmer; the dashed lines correspond to the magnetic moment of $m - \delta m$ and $m + \delta m$ which are the upper and lower limits for magnetic moment extracted from distribution of the size and number of magnetosomes in TEM images (see Materials and methods - “Magnetic moment measurement” for details).

The analysis in Fig. 4b also indicates (and makes use of) the large cell-to-cell variability with respect to the swimming velocity and the magnetic moment. The large heterogeneity of swimming velocities is also shown by the histogram in Supplementary Fig. 10. The variability of the magnetic moment can be estimated from the distribution of the numbers and sizes of magnetosomes in TEM images (see Materials and methods - “Magnetic moment measurement” and supplementary Figures 11, 12 and 13), which results in a range $m \pm \delta m$ of magnetic moments and a corresponding range of U-turn radii, indicated by the two dashed black lines in Fig. 4b. Notably, almost all measured U-turn radii fall into this range which further validates our model.

The U-turn behavior is also reflected in the radial distribution of the bacteria, where U-turns lead to a second, smaller peak towards the center of the trap that is absent without a magnetic field, as seen in both simulations and experiments (Fig. 5a and b, respectively). Here it is important to stress that this peak is not seen in the population-averaged distribution, but only for individual bacteria (see Supplementary Fig. 14), again due to the heterogeneity in bacterial parameters. Thus, single-cell analysis is crucial for a quantitative understanding of the mechanisms underlying these trajectories. We also note that the position and width of the main peak towards the exterior of the trap are unaffected by the magnetic field, indicating that the interactions with the wall (meaning, the parameters A_w and T_w) are not influenced by the presence of a magnetic field.

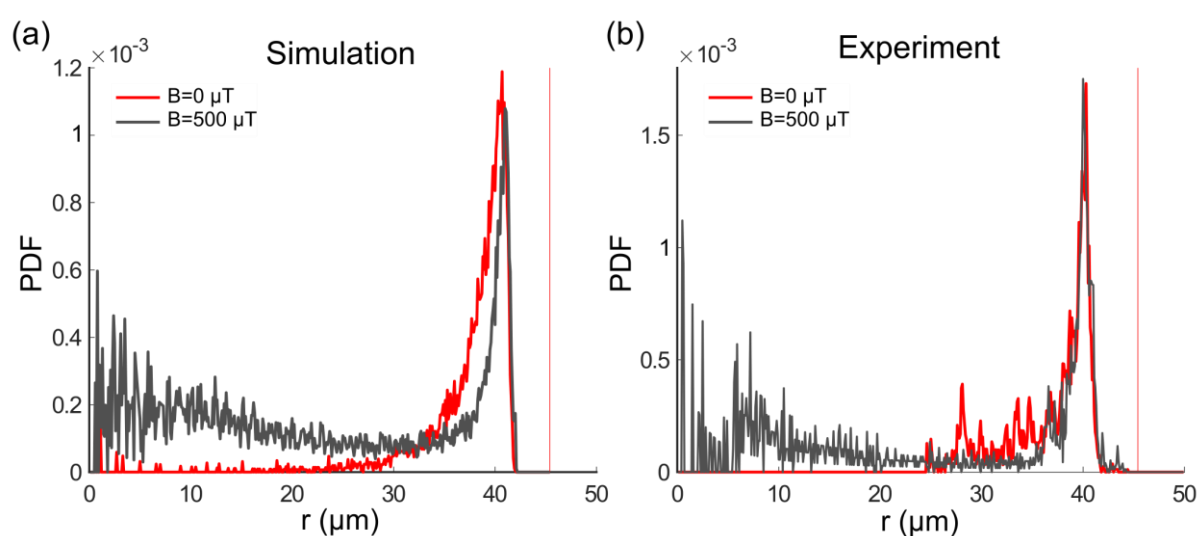


Fig. 5. Single cell Radial distribution (PDF) in the absence of magnetic field (red) and with a magnetic field of 500 μT (grey) for the microfluidic trap size 45 μm , showing both the simulation (a) and experimental data (b), with a mean velocity of 40 $\mu\text{m s}^{-1}$. The vertical red dotted line represents the wall position.

Conclusions

In this study, we have investigated the swimming behavior of individual magnetotactic bacteria trapped in micron-sized compartments, in particular the interplay between their interaction with the confining walls and an external magnetic field guiding their motion. This unique combination of micro-sized confinement within a controllable magnetic field has allowed us to observe a variety of behaviors and to compare the data to a theoretical model. Two notable results emerged from these observations and from their theoretical analysis. On the one hand, we showed that the variety of observed behaviors could be explained by a rather simple physical description, based on the balance of two torques, the magnetic torque and a wall torque arising from the interaction with the trap walls. On the other hand, our observations reveal a large heterogeneity in the bacterial population with respect to parameters of the motility as well as the magnetic properties, in agreement with previous results^{41,56,57}.

As a result of that heterogeneity, the swimming behavior of these bacteria is blurred by observations at the population level, and single-cell observations and quantification are crucial for a full understanding of bacterial motility. The microfluidic trapping approach used in this work provides such quantitative single-cell characterization and may be extended to the quantification of other parameters of motility (e.g. rates of pausing or reversals, and chemotactic behaviors) as well as other processes including cell division and possibly flagellum assembly. Experimental challenges of this approach include the trap realization and closure as well as the video analysis, which required stabilization. Our platform is able to provide a reproducible trap volume in which we can define the dimensions for comparison to the simulated data. This is in contrast to confinement within microfluidic droplets for example where the bacteria can swim in 3-D²⁹ and imaging of the single trajectories can prove to be difficult.

In the absence of a magnetic field, the observed behavior of the trapped bacteria was seen to be rather similar to that observed for single-cell algae in an earlier study³¹. In particular, in both cases, circling around the wall perimeter was observed, indicating a similar interaction with the wall despite the hydrodynamic differences between the organisms. This similarity might therefore indicate that steric effects dominate the interactions with the walls, but more detailed studies of the hydrodynamic interactions with the walls or comparisons with other types of microswimmers will be needed to draw definite conclusions.

In contrast to algae, however, the magnetotactic bacteria can be steered “remotely” with a magnetic field: one of the reasons why they are attractive candidate microswimmers for biomedical and environmental applications. Our observations show that steering magnetotactic bacteria needs to take the interactions with channel walls or obstacles into account, a situation expected to be rather

frequent in application scenarios. However, they also show that if interactions with walls are taken into account, the interplay of simple physical forces can quantitatively explain and predict the swimming behavior. It will be interesting to generalize this result to other types of biological and synthetic magnetic microswimmers. For example, a completely different system of synthetic rollers confined in a circular geometry and subjected to flows⁵⁸ shows similar behavior to the one portrayed in this study, hinting at the flexibility of this approach.

In summary, we have shown how magnetic torques and torques due to interactions with confining walls direct the motion of bacteria in microfluidic traps, which provide a way to quantitatively address the individuality of the bacteria and thereby to obtain a more complete understanding of the physics and biology of their swimming. The study of the swimming in a defined structure will be useful for the future understanding of their behavior in more complex systems, including the porous environment in the sediment habitats or in biomedical application scenarios. Likewise, the microfluidic trapping approach may also be a useful tool for studying other species of microorganisms and synthetic microswimmers as well as other biological processes.

Materials and methods

Computational modeling

The simulation is based on an Active Brownian Particle method (ABP) in 3 dimensions³³. Bacteria are represented by spheres, whose single trajectories are simulated by integrating the following equations:

$$\gamma_t \frac{d\mathbf{r}}{dt} = \gamma_t v \mathbf{e} + \mathbf{F}_{WCA} + \sqrt{2k_B T \gamma_t} \xi_t \quad (3)$$

$$\gamma_r \frac{d\mathbf{e}}{dt} = [\mathbf{m} \times \mathbf{B} + T_{\text{reor.}} + \sqrt{2k_B T \gamma_r} \xi_r] \times \mathbf{e}, \quad (4)$$

where t is the time, \mathbf{r} is the position of the bacterium, \mathbf{e} is the direction vector, T is the temperature, k_B is the Boltzmann constant, γ_t and γ_r the translational and rotational friction coefficients, respectively, v is the speed of self propulsion, $\mathbf{m} \times \mathbf{B}$ is the external magnetic torque with m being the magnetic moment of the bacterium and \mathbf{B} the external magnetic field, \mathbf{F}_{WCA} and $T_{\text{reor.}}$ are the force and reorientation torque due to the interaction with the wall (see the following paragraph) and ξ_t and ξ_r describe uncorrelated white noise in the translational and rotational degrees of freedom.

The trap is composed of a lateral curved wall and two flat surfaces (bottom and ceiling), with dimensions match those of the experimental ones. The wall interaction is implemented as follows (see Fig. 15 in the supplementary materials). An imaginary sphere of radius A_w is positioned with its center on the wall. The bacterium, represented as a sphere of radius a , interacts with the imaginary sphere and therefore is repelled by a Weeks-Chandler-Andersen potential (WCA) potential^{31,59} which gives a force perpendicular to the wall and directed towards the center of the trap:

$$\mathbf{F}_{WCA} = \begin{cases} -24\epsilon \frac{\hat{r}}{|\mathbf{r}|} \left[2 \left(\frac{\sigma}{|\mathbf{r}|} \right)^{12} - \left(\frac{\sigma}{|\mathbf{r}|} \right)^6 \right] & \text{for } |\mathbf{r}| < \sigma 2^{1/6} \\ 0 & \text{otherwise} \end{cases} \quad (5)$$

where ϵ is the strength of the force set to 10^{-10} (to avoid unphysical interactions such as bacteria entering the walls), \mathbf{r} , \hat{r} , $|\mathbf{r}|$ are respectively the vector between the center of the imaginary sphere and the center of the bacterium ($\mathbf{x}_{\text{im.sphere}} - \mathbf{x}_{\text{bact.}}$), its unit vector and its modulus, and $\sigma = \frac{a+A_w}{2^{1/6}}$ with a the radius of the bacterium. Moreover, upon interaction with the wall, the bacterium feels a reorientation torque:

$$T_{\text{reor.}} = T_w \mathbf{e} \times \mathbf{F}_{WCA}, \quad (6)$$

where T_w is the strength of the torque. Hydrodynamics is not considered explicitly in the model, but is included indirectly in the effective reorientation torque. The free parameters are A_w and T_w , which depend on the radius of the trap (thus on the curvature) but not on the magnetic properties of the system. These parameters are determined by comparison with the experiments as illustrated in the materials and method section ‘Fitting of the radial distribution’.

Fabrication of the master molds and microfluidic systems

Two silicon wafers were used as master molds for the final PDMS chips; one for the upper control layer and one for the lower fluidic layer. The silicon wafers were initially baked at 200 °C for 20 min and were allowed to cool down to room temperature. For the control layer, a SU-8 3010 (MicroChem Inc.) thin film was spin-coated onto the wafer to a height of 20 μm, baked and exposed to UV light through a film mask (Micro Litho) with a mask aligner (Kloé UV-KUB 3) according to the manufacturer recommendations. For the fluidic layer, multilayer photolithography was employed. First, an initial SU-8 3010 10 μm film was spin-coated onto the wafer, baked and exposed according to the manufacturer recommendations. Then, another SU-8 3010 10 μm film was spin-coated, baked and exposed (with a second mask) again according to the manufacturer recommendations, but with a slight variation in the spin-coating parameters, where the spin speed was increased to achieve a 75% of the target height resulting in a height of 10 μm. The wafers were then developed with mr-Dev 600 (microresist technologies). A more detailed description of the wafer fabrication parameters can be found in the Supplementary Table 4. The SU-8 film height was measured with a white light interferometer (Wyko NT1100). Prior to their use, the master molds were treated with 1H,1H,2H,2H-perfluorodecyltriethoxysilane 97% (abcr) to reduce PDMS adhesion upon usage.

The final two-layered microfluidic device was produced with (PDMS) via soft lithography. Briefly, PDMS elastomer monomer and curing agent (Sylgard 184, Dow Corning) were mixed in a ratio 10:1 and then degassed. For the fabrication of the control layer, the PDMS was cast onto the master mold to a height of about 5 mm and cured at 80 °C for 2 h. For the fluidic layer, the PDMS was spin-coated onto the master mold until reaching a thickness of 40 μm (spinning at 500 rpm for 30s, then 2,000 rpm for 60 s), and cured at 80 °C for 1 h. The inlets for the control layer were then punched with a 1 mm diameter biopsy punch (pmfmedical). The control and fluidic layers were plasma treated, aligned and then bonded. Subsequently, the fluidic layer inlet and outlet were punched with a 1.5 mm diameter biopsy punch. Finally, the PDMS assembly and a clean glass coverslip were bonded by plasma activation to finish the microfluidic device (Supplementary Figure 2b).

Operation of the chip

The control and fluidic layers were filled by centrifugation for 10 min at 900 RCF with MSR-1 growth medium or milliQ water. The control layer was connected to a pressurized nitrogen source connected through a series of silicon tubing (I.D. = 1 mm, Roth) to a custom-built valve device⁶⁰. The silicon tubing was inserted into the microfluidic inlets by means of a metal connector. The fluidic layer was connected by a metal connector to a PTFE tubing (I.D. = 0.8 mm, Saint-Gobain Performance Plastics Isofluor GmbH) which connected the device to a 1 mL plastic syringe (Norm-Ject, Henke-Sass Wolf) filled with a bacterial suspension or with calcein. The syringe was loaded onto a mechanical syringe pump (Aladdin, WPI) and liquid was dispensed into the microfluidic system at a flow rate of 5 μ L/min. For closing the microfluidic traps, the valves were actuated by applying a pressure of 1.75 bar with nitrogen (Supplementary Figure 2).

Selection of magnetic motile bacteria

MSR-1 was cultured in MSR-1 growth medium with the composition indicated by Heyen and Schüler⁶¹, with the addition of pyruvate (27 mM) as carbon source instead of lactate. For the creation of an aerotactic band and the subsequent selection of swimming bacteria, the growth medium was supplemented with 0.1% agar. Briefly, 1 mL of bacteria was inoculated into the bottom of a 15 mL Hungate tube filled with 10 mL of MSR-1 growth medium with 0.1% agar. The tube was sealed with a rubber cap pierced with a needle capped with a 0.2 μ m filter (Whatman) to allow the formation of an oxygen gradient. To have the north-seeking bacteria (i.e. swimming with the north of their magnet at their front in oxic conditions) in the formed band, the tube was put inside a pair of coils to apply a magnetic field parallel to the oxygen gradient, but pointing downwards to the anoxic region (equivalent to the situation that the bacteria experience in their natural habitat in the Northern Hemisphere). The bacteria were grown at 28 °C and allowed to form an aerotactic band. Once the band had formed, the motile bacteria were selected by harvesting the band and culturing them for two passes in standard MSR-1 growth medium and microaerobic conditions. Subsequently, the magnetic bacteria were collected with a needle by placing a magnet next to the tube to attract them. The final population of north-seeking bacteria was estimated to be about 80% of the population. In oxic conditions as in our experiment (where oxygen can freely diffuse through the PDMS into the trap), these bacteria swim with the north of their magnet at their front. Nevertheless, few traps contained south seekers, swimming with the south of their magnet at their front, and thus they were excluded from the subsequent analysis. The optical density was measured at 565 nm (OD_{565}) and was adjusted as needed with fresh growth medium for subsequent measurements.

Microscopy and image stabilization

Bacteria confined within the microfluidic traps were imaged on a custom inverted microscope¹⁴ using a long working distance 40x objective lens (NA=0.6, air, Nikon) and an sCMOS camera (2560×2160 pixels; Zyla, Andor Technology). The sample was illuminated with white light by an LED illumination system pE-4000 (CoolLED Ltd, Andover, UK). Images were captured with Andor iQ3 software at a pixel size of 111 nm/pixel, and saved as a 16-bit tiff stack. Each stack consisted of 2,000 slices per experiment, with 20 ms time step between slices.

The microscope was equipped with 3D-axis Helmholtz coils with a controller (C-SpinCoil-XYZ, Micro Magnetics Inc.). These coils were used to apply DC magnetic fields with a precision of $\pm 2.5 \mu\text{T}$ (5% of the Earth's magnetic field). A photo of the microscope platform and the 3D-axis Helmholtz coils is shown in Supplementary Fig. 16. A 3-axis magnetic sensor (Micro Magnetics Inc.) was used to measure the precise value of the Earth's magnetic field in sample location. The magnetic field was controlled using a LabVIEW (National Instruments) based program and the ambient magnetic field was canceled out before each experiment. The magnetic field was then set to 0 μT , 50 μT or 500 μT parallel to the microfluidic trap diameter (inset of Supplementary Fig. 16). The microscope was equipped with three motorized linear stages (Z825B, Thorlabs) to provide sample positioning in 3D.

Due to the micron-size of the microfluidic traps and the fact that the bacteria tend to swim near the walls, even a small amount of vibration hinders correct background subtraction and consequently the bacteria tracking process. Therefore, a custom-made script was developed in MATLAB (MathWorks, Inc.) for image stabilization and background subtraction. The image stabilization was based on comparing two successive frames and detecting the corners and features that were sharp and changed drastically (the green crosses in Supplementary Fig. 17c,d). Then matched points were detected and connected, and transformation (including scaling, rotation, translation, and shearing) was applied to the image to overlay the points (Supplementary Fig. 17e,f). An effective background subtraction, and hence tracking of the bacteria, could be achieved after image stabilization (Supplementary Fig. 17g,h).

Microfluidic trap characterization

A total number of 5 different microfluidic trap dimensions with radii of 7.5, 12.5, 17.5, 25, and 45 μm are used. To determine the actual microfluidic traps dimensions, the microfluidic traps were imaged with a confocal laser scanning microscope (SP8 DMI8, Leica) equipped with 63x objective (water immersion, N.A.=1.2, Leica). For this purpose, the fluidic and control layers were initially filled with milliQ water. The water in the fluidic layer was then exchanged with a fluorescent solution containing 25 μM of calcein and 10 mM HEPES at pH 7.0, and the valves were subsequently actuated to close the traps. For each size, 10 microfluidic traps were imaged and z-stack including 50 z positions were

recorded with a 488 nm laser with a z-stack height of 356 nm per microfluidic trap. The microfluidic trap radii were determined by fitting a circle to the fluorescent area (Supplementary Fig. 18, and Table 1). The height was determined by multiplying the number of z-stacks bearing a fluorescent signal by the z-stack height.

Bacterial imaging

Initially, the control layer and the fluidic layer of the microfluidic device were filled with MSR-1 growth medium. A bacterial suspension with the required OD_{565} was then loaded into the microfluidic device at a flow rate of $5 \mu\text{L min}^{-1}$. Once the bacterial suspension had reached the fluidic channels (under the traps), the flow was stopped and the valves were lowered with 1.75 bar pressure, thus confining bacteria in the closed microfluidic traps. The experiments were conducted with all available five different microfluidic trap dimensions (subsection: Microfluidic trap characterization). Each experiment was recorded for 40 seconds (2,000 frames with 50 fps). The experiments were repeated 5 to 8 times independently, with different microfluidic traps and bacteria for each trap size, which corresponds to roughly 10^4 total trajectory points. The final number of bacteria inside the microfluidic trap can be tuned by controlling the initial concentration of the bacterial suspension (Supplementary Fig. 3). For the trap sizes of radius 7.5, 12.5 and $17.5 \mu\text{m}$, microfluidic traps with only one bacterium were selected to avoid bacterium-bacterium interactions. However, for traps of radius 25 and $45 \mu\text{m}$, the videos were recorded with a maximum of 2 and 4 bacteria per trap, respectively. The microfluidic traps were opened and washed out every 10 minutes by fresh medium and bacteria.

Prior to each measurement, the magnetotactic behavior of the bacteria was inspected by applying a rotating magnetic field of 1 mT to the sample. Only bacteria showing a magnetic field-dependent response were recorded. The rotating magnetic field was shown not to alter the posterior swimming behavior of the bacteria.

Bacterial tracking

Bacteria tracking in 2D was performed using custom-made scripts in MATLAB, after image stabilization and background subtraction (see Supplementary Fig. 17). The bacteria were identified based on an intensity threshold and their locations were determined by finding a centroid of contiguous pixels in a region with intensity above this level. The trajectories were formed by connecting centroid positions in subsequent frames. Resulting trajectories were smoothed with a five-point moving average (Supplementary Fig. 4, and Supplementary Video 1). The points resulting from the incorrect tracking of the wall were discarded by applying a cutoff circle with radius of 1.1 times the radius of the trap according to the thickness of trap wall shadow in the recorded images (see Supplementary Fig. 4). For

the trap with $7.5 \mu\text{m}$ radius, the tracks were obtained by hand through the help of a self-written MATLAB code, since the automatic tracking gave poor results. The instantaneous fourth order velocities along the trajectories were calculated for all trajectories. The experiments at a given condition (radius and magnetic field) were repeated for 6 to 8 different microfluidic traps, each containing different bacteria.

Data analysis

The trajectories, both experimental and simulated, are processed and analyzed in the same way. In particular, the U-turn radii, the distribution of the bacteria, and the heat maps were extracted as follows.

U-turns

The U-turns are identified through a semi-manual algorithm adapted from ⁶² to measure the U-turn radius, a circle is fitted on the manually-selected portion of the track presenting a U-turn. The mean U-turn radius is then obtained for each trap. For the experimental trajectories only, the corresponding velocity of the bacterium when performing the U-turn was measured by averaging over instantaneous velocities in that segment of the trajectory (Supplementary Fig. 19). Sample U-turns in different traps sizes in the presence of $500 \mu\text{T}$ of magnetic field are shown in Supplementary Fig. 20.

Radial distributions

To calculate the radial distribution, the trap is divided into concentric rings of width $\Delta r = 0.1$. Then, the radial distribution function of the trap occupancy is determined by counting the number n of frames where a bacterium is in a shell with thickness of Δr at a distance of r from the center of the trap, and averaging over the total number of bacteria in different traps of the same size N , resulting in a probability density function (PDF) of $n/(N2\pi r\Delta r)$ ³¹. The distribution for each value of magnetic field and trap size was obtained as a mean over the single traps, and the error is given by one standard deviation.

Heat-map

To visualize the high-density points in the traps, a heat-map was produced by binning areas of $1\mu\text{m} \times 1\mu\text{m}$, calculating the number of points of the tracks in the bin, and normalizing by the bin area and the total number of points.

Fitting of the radial distribution

In the simulation, there are two free parameters: the interaction range A_w (which gives an indication of the distance from the wall at which hydrodynamics acts and thus mainly influences the peak position) and the strength of a wall torque T_w . These free parameters are changed until the simulated curve matches the experimental radial distribution, and the final parameters are the ones minimizing the adjusted R squared between the experimental and simulated curve (written in MATLAB, Mathworks Inc.) $R_{adj}^2 = 1 - \frac{n-1}{v} \frac{\sum(\exp-sim)^2}{\sum(\exp-exp)^2}$, where n is the number of points and $v=2$ is the number of free parameters, exp is the arithmetic mean of the experimental data and sim is the simulated data. While the match is good for bigger microfluidic traps (with an adjusted R squared of 0.896 for the microfluidic trap with radius of $45\mu m$, see inset of Fig. 2), it gets poorer for smaller microfluidic traps (0.702 for the microfluidic trap with radius of $7.5\mu m$ where manual tracking is used and 0.508 for the microfluidic trap with radius of $11.5\mu m$ where the automatic tracking is used), due to the righthand tail of the distribution of the experimental data. For the small microfluidic traps, the distribution is broader on the wall side of the peak, possibly due to irregularities of the overall trap shape of the microfluidic trap and because of slight variations in the microfluidic trap radius, the effects become more prominent for small traps. Excluding the smallest trap where manual tracking was used, the righthand tail could be increased by artefacts of the algorithm which recognizes bright parts of the wall as a bacterium.

Bacterial magnetosome counting

The number and diameter of the magnetosomes were computed from the TEM 2D images using a semi-automatic custom-made application in MATLAB. For each image, the user had to manually draw a region of interest (ROI) to delimit the boundary of each bacteria. These ROIs were used to count the magnetosomes separately for each bacterium and to avoid artefacts that could be found outside the cell. A build-in MATLAB function based on Circular Hough Transform⁶³ was used to automatically find the number of magnetosomes and their sizes. Manual filtering of artefacts was possible when the automatic segmentation failed.

Magnetic moment measurement

The magnetic moments of the bacteria were determined by examining the number and diameter of magnetosomes inside the bacteria by transmission electron microscopy (TEM). TEM grids were prepared by adding 20 μL of bacterial suspension and letting them settle down during 30 min before washing them twice with milliQ water and drying them with paper. TEM images were taken with a

transmission electron microscope (EM912, Zeiss) at an accelerating voltage of 120 kV with a magnification of 4,000-10,000x.

The variability of the magnetic moment can be estimated from the distribution of the numbers and sizes of magnetosomes in the TEM images (see Supplementary Figures 11, 12 and 13). According to the data of TEM images (Supplementary Figure 11), the mean value of the number of magnetosomes inside bacteria is $N = 23.8 \pm 8.3$ (Supplementary Figure 12) and the mean size of magnetic nano crystals is $R = 19.4 \pm 4.3$ nm (Supplementary Figure 13). The magnetosome diameters were calculated by fitting a circle to the magnetosome TEM images. Therefore, the mean value and the error of the magnetic moment are:

$$M = N \frac{4}{3} \pi R^3 \rho_M = 3.54 \times 10^{-16} Am^2 \quad (7)$$

$$\delta M = |M| \sqrt{\left(\frac{\delta N}{N}\right)^2 + \left(3 \frac{\delta R}{R}\right)^2} = 0.75M \quad (8)$$

Here, ρ_M is magnetic moment per unit volume of magnetite which is equal to $4.8 \times 10^{-22} \frac{A.m^2}{nm^3}$ ⁶⁴. N is the average number of magnetosomes inside magnetosome chain with the standard deviation of δN . R and δR stand for the mean radius of magnetosomes and the corresponding error, respectively. As the number of magnetosomes in the chain and the magnetosomes sizes are widely distributed, we calculate the highest and lowest possible magnetic moment of the chain. Based on equations (7) and (8), the expected value for the magnetic moment of the bacteria is included between the values $\pm 0.75M$.

Contributions

A.C., D.F., T.R., and S.K. designed research. A.C. wrote the code, performed the simulations and analyzed the simulated data; E.C.-D. designed and produced the microfluidic channels; E.C.-D. and M.A.C. performed the experiments and analyzed the experimental data; M.A.C. developed image processing algorithms to enhance videos and track bacteria. H.M.T developed a script to analyse the number of magnetosomes and their size in a bacterium. All authors discussed the results and wrote the manuscript.

Acknowledgements

The authors thank Heike Runge for taking the TEM images. This work was supported by the Deutsche Forschungsgemeinschaft within the Priority Program 1726 on microswimmers (grant No. FA 835/7-1 and KL 818/2-1 to D.F. and S.K.). T.R. acknowledges support from the MaxSynBio consortium which is jointly funded by the Federal Ministry of Education and Research of Germany and the Max Planck

Society. A.C., E.C.D. and H.M.T. were supported by the IMPRS on Multiscale Biosystems. The funders had no role in study design, data collection and analysis, decision to publish, or preparation of the manuscript.

References

1. Bechinger, C. *et al.* Active Particles in Complex and Crowded Environments. *Rev. Mod. Phys.* **88**, 045006 (2016).
2. Ezhilan, B. *et al.* On the distribution and swim pressure of run-and-tumble particles in confinement. *J. Fluid Mech.* **781**, (2015).
3. Lauga, E. & Powers, T. R. The hydrodynamics of swimming microorganisms. *Reports Prog. Phys.* **72**, 96601 (2009).
4. Peyer, K. E., Zhang, L. & Nelson, B. J. Bio-inspired magnetic swimming microrobots for biomedical applications. *Nanoscale* **5**, 1259–1272 (2013).
5. Magdanz, V. & Schmidt, O. G. Spermibots: potential impact for drug delivery and assisted reproductive technologies. *Expert Opin. Drug Deliv.* **11**, 1125–1129 (2014).
6. Schwarz, L., Medina-Sánchez, M. & Schmidt, O. G. Hybrid BioMicromotors. *Applied Physics Reviews* vol. 4 31301 (2017).
7. Bente, K., Codutti, A., Bachmann, F. & Faivre, D. Biohybrid and Bioinspired Magnetic Microswimmers. *Small* **14**, 1704374 (2018).
8. Ford, R. M. & Harvey, R. W. Role of chemotaxis in the transport of bacteria through saturated porous media. *Adv. Water Resour.* **30**, 1608–1617 (2007).
9. Timmis, K. N. & Pieper, D. H. Bacteria designed for bioremediation. *Trends Biotechnol.* **17**, 201–204 (1999).
10. Pieper, D. H. & Reineke, W. Engineering bacteria for bioremediation. *Current Opinion in Biotechnology* vol. 11 262–270 (2000).
11. Felfoul, O. *et al.* Magneto-aerotactic bacteria deliver drug-containing nanoliposomes to tumour hypoxic regions. *Nat. Nanotechnol.* **11**, 941–947 (2016).
12. Felfoul, O., Becker, A. T., Fagogenis, G. & Dupont, P. E. Simultaneous steering and imaging of magnetic particles using MRI toward delivery of therapeutics. *Sci. Rep.* **6**, 33567 (2016).
13. Sherwood, J. L. *et al.* Analysis of bacterial random motility in a porous medium using magnetic resonance imaging and immunomagnetic labeling. *Environ. Sci. Technol.* **37**, 781–785 (2003).
14. Bennet, M. *et al.* Influence of Magnetic Fields on Magneto-Aerotaxis. *PLoS One* **9**, e101150 (2014).
15. Lefèvre, C. T. *et al.* Diversity of magneto-aerotactic behaviors and oxygen sensing mechanisms

- in cultured magnetotactic bacteria. *Biophys. J.* **107**, 527–538 (2014).
16. Popp, F., Armitage, J. P. & Schüler, D. Polarity of bacterial magnetotaxis is controlled by aerotaxis through a common sensory pathway. *Nat. Commun.* **5**, 5398 (2014).
 17. Duffy, K. J., Cummings, P. T. & Ford, R. M. Random walk calculations for bacterial migration in porous media. *Biophys. J.* **68**, 800–806 (1995).
 18. Dillon, R., Fauci, L. & Gaver, D. A microscale model of bacterial swimming, chemotaxis and substrate transport. *J. Theor. Biol.* **177**, 325–340 (1995).
 19. Torkzaban, S., Tazehkand, S. S., Walker, S. L. & Bradford, S. A. Transport and fate of bacteria in porous media: Coupled effects of chemical conditions and pore space geometry. *Water Resour. Res.* **44**, (2008).
 20. Reichhardt, C. & Olson Reichhardt, C. J. Active matter transport and jamming on disordered landscapes. *Phys. Rev. E - Stat. Nonlinear, Soft Matter Phys.* **90**, 012701 (2014).
 21. Raatz, M., Hintsche, M., Bahrs, M., Theves, M. & Beta, C. Swimming patterns of a polarly flagellated bacterium in environments of increasing complexity. *Eur. Phys. J. Spec. Top.* **224**, 1185–1198 (2015).
 22. Theves, M., Taktikos, J., Zaburdaev, V., Stark, H. & Beta, C. Random walk patterns of a soil bacterium in open and confined environments. *EPL (Europhysics Lett.)* **109**, 28007 (2015).
 23. Dehkharghani, A. Hindered Transport of Bacteria in Porous Media Flows. (Tufts University, 2017).
 24. Anbari, A. *et al.* Microfluidic Model Porous Media: Fabrication and Applications. *Small* **14**, 1703575 (2018).
 25. Aleklett, K. *et al.* Build your own soil: Exploring microfluidics to create microbial habitat structures. *ISME Journal* vol. 12 312–319 (2018).
 26. Reichhardt, C. J. O. & Reichhardt, C. Ratchet Effects in Active Matter Systems. *Annu. Rev. Condens. Matter Phys.* **8**, 51–75 (2017).
 27. Galajda, P., Keymer, J., Chaikin, P. & Austin, R. A wall of funnels concentrates swimming bacteria. *J. Bacteriol.* **189**, 8704–8707 (2007).
 28. Wan, M. B., Olson Reichhardt, C. J., Nussinov, Z. & Reichhardt, C. Rectification of swimming bacteria and self-driven particle systems by arrays of asymmetric barriers. *Phys. Rev. Lett.* **101**, 018102 (2008).
 29. Vincenti, B. *et al.* Magnetotactic bacteria in a droplet self-assemble into a rotary motor. *Nat. Commun.* **10**, 5082 (2019).
 30. Kühn, M. J., Schmidt, F. K., Eckhardt, B. & Thormann, K. M. Bacteria exploit a polymorphic instability of the flagellar filament to escape from traps. *Proc. Natl. Acad. Sci. U. S. A.* **114**, 6340–6345 (2017).

31. Ostapenko, T. *et al.* Curvature-guided motility of microalgae in geometric confinement. *Phys. Rev. Lett.* **120**, 068002 (2018).
32. Hassan, H. A., Pichely, M., Hagemany, T., Abelmannyz, L. & Khali, I. S. M. Influence of the magnetic field on the two-dimensional control of *Magnetospirillum gryphiswaldense* strain MSR-1. in *IEEE International Conference on Intelligent Robots and Systems* vols 2016- November 5119–5124 (Institute of Electrical and Electronics Engineers Inc., 2016).
33. Codutti, A., Bente, K., Faivre, D. & Klumpp, S. Chemotaxis in external fields: Simulations for active magnetic biological matter. *PLoS Comput. Biol.* **15**, e1007548 (2019).
34. Frankel, R. B., Williams, T. J. & Bazylinski, D. A. Magneto-Aerotaxis. in *Magnetoreception and Magnetosomes in Bacteria* 1–24 (Springer Berlin Heidelberg, 2006). doi:10.1007/7171_2006_036.
35. Frankel, R. B. Magnetic Guidance of Organisms. *Annu. Rev. Biophys. Bioeng.* **13**, 85–103 (1984).
36. Bente, K. *et al.* High-speed motility originates from cooperatively pushing and pulling flagella bundles in bilophotrichous bacteria. *bioRxiv* (2019) doi:10.1101/629121.
37. Park, B. W., Zhuang, J., Yasa, O. & Sitti, M. Multifunctional Bacteria-Driven Microswimmers for Targeted Active Drug Delivery. *ACS Nano* **11**, 8910–8923 (2017).
38. Vach, P. J. *et al.* Selecting for function: Solution synthesis of magnetic nanopropellers. *Nano Lett.* **13**, 5373–5378 (2013).
39. Peyer, K. E., Tottori, S., Qiu, F., Zhang, L. & Nelson, B. J. Magnetic helical micromachines. *Chem. - A Eur. J.* **19**, 28–38 (2013).
40. Huang, G. & Mei, Y. Helices in micro-world: Materials, properties, and applications. *Journal of Materiomics* vol. 1 296–306 (2015).
41. Stanton, M. M. *et al.* Magnetotactic Bacteria Powered Biohybrids Target E. coli Biofilms. *ACS Nano* **11**, 9968–9978 (2017).
42. Thorsen, T., Maerkl, S. J. & Quake, S. R. Microfluidic large-scale integration. *Science (80-.)*. **298**, 580–584 (2002).
43. Robinson, T., Kuhn, P., Eyer, K. & Dittrich, P. S. Microfluidic trapping of giant unilamellar vesicles to study transport through a membrane pore. *Biomicrofluidics* **7**, (2013).
44. Murat, D. *et al.* Opposite and coordinated rotation of amphitrichous flagella governs oriented swimming and reversals in a magnetotactic spirillum. *J. Bacteriol.* **197**, 3275–3282 (2015).
45. Romanczuk, P., Bär, M., Ebeling, W., Lindner, B. & Schimansky-Geier, L. Active Brownian particles: From individual to collective stochastic dynamics: From individual to collective stochastic dynamics. *European Physical Journal: Special Topics* vol. 202 1–162 (2012).
46. Kalinin, Y. V., Jiang, L., Tu, Y. & Wu, M. Logarithmic sensing in *Escherichia coli* bacterial

- chemotaxis. *Biophys. J.* **96**, 2439–2448 (2009).
47. Khatami, M., Wolff, K., Pohl, O., Ejtehadi, M. R. & Stark, H. Active Brownian particles and run-and-tumble particles separate inside a maze. *Sci. Rep.* **6**, (2016).
 48. Takatori, S. C., Yan, W. & Brady, J. F. Swim pressure: Stress generation in active matter. *Phys. Rev. Lett.* **113**, (2014).
 49. Perez Ipiña, E., Otte, S., Pontier-Bres, R., Czerucka, D. & Peruani, F. Bacteria display optimal transport near surfaces. *Nat. Phys.* **15**, 610–615 (2019).
 50. Berdakin, I. *et al.* Influence of swimming strategy on microorganism separation by asymmetric obstacles. *Phys. Rev. E - Stat. Nonlinear, Soft Matter Phys.* **87**, 052702 (2013).
 51. Berdakin, I., Silhanek, A. V., Moyano Cortéz, H. N., Marconi, V. I. & Condat, C. A. Quantifying the sorting efficiency of self-propelled run-and-tumble swimmers by geometrical ratchets. *Cent. Eur. J. Phys.* **11**, 1653–1661 (2013).
 52. Guidobaldi, H. A. *et al.* Disrupting the wall accumulation of human sperm cells by artificial corrugation. *Biomicrofluidics* **9**, 024122 (2015).
 53. Codutti, A. Behavior of magnetic microswimmers : simulations for natural swimmers and synthetic propellers, PhD Thesis. (Universität Potsdam, 2018). doi:10.25932/publishup-42297.
 54. Telezki, V. & Klumpp, S. Simulations of structure formation by confined dipolar active particles. *Soft Matter* **16**, 10537–10547 (2020).
 55. ESQUIVEL, D. M. S. & LINS DE BARROS, H. G. P. Motion of Magnetotactic Microorganisms. *J. Exp. Biol.* **121**, (1986).
 56. Wang, M. & Ford, R. M. Transverse bacterial migration induced by chemotaxis in a packed column with structured physical heterogeneity. *Environ. Sci. Technol.* **43**, 5921–5927 (2009).
 57. Mitchell, J. G. & Kogure, K. Bacterial motility: links to the environment and a driving force for microbial physics. *FEMS Microbiol. Ecol.* **55**, 3–16 (2006).
 58. Morin, A. & Bartolo, D. Flowing Active Liquids in a Pipe: Hysteretic Response of Polar Flocks to External Fields. *Phys. Rev. X* **8**, 021037 (2018).
 59. Weeks, J. D., Chandler, D. & Andersen, H. C. Role of repulsive forces in determining the equilibrium structure of simple liquids. *J. Chem. Phys.* **54**, 5237–5247 (1971).
 60. Kubsch, B., Robinson, T., Steinkühler, J. & Dimova, R. Phase behavior of charged vesicles under symmetric and asymmetric solution conditions monitored with fluorescence microscopy. *J. Vis. Exp.* **2017**, 56034 (2017).
 61. Heyen, U. & Schüller, D. Growth and magnetosome formation by microaerophilic *Magnetospirillum* strains in an oxygen-controlled fermentor. *Appl. Microbiol. Biotechnol.* **61**, 536–544 (2003).
 62. Thageman. Bacteria tracker and Uturn analyzer. *MATLAB Central File Exchange*

<https://www.mathworks.com/matlabcentral/fileexchange/64498-bacteria-tracker-and-uturn-analyzer> (2020).

63. Atherton, T. J. & Kerbyson, D. J. Size invariant circle detection. *Image Vis. Comput.* **17**, 795–803 (1999).
64. CRC Handbook of Chemistry and Physics: A Ready-Reference of Chemical and Physical Data, 85th ed Edited by David R. Lide (National Institute of Standards and Technology). CRC Press LLC: Boca Raton, FL. 2004. 2712 pp. \$139.99. ISBN 0-8493-0485-7. *J. Am. Chem. Soc.* **127**, 4542–4542 (2005).